



Rational synthesis of sea urchin-like NiCo-LDH/tannin carbon microsphere composites using microwave hydrothermal technique for high-performance asymmetric supercapacitor

Weigang Zhao¹ · Jianping Deng¹ · Menghan Li¹ · Guanben Du² · Mizi Fan³ · Haili Gao¹ · Zhanhui Yuan¹

Received: 4 October 2024 / Revised: 11 December 2024 / Accepted: 6 January 2025
© The Author(s) 2025

Abstract

In this study, tannin-derived porous carbon (TAC) with different microstructures was prepared via a microwave hydrothermal method, followed by KOH activation. Subsequently, the sea urchin-like NiCo-LDH/Tannin-derived carbon-based microsphere composite materials were rationally synthesized through a single-step microwave hydrothermal co-assembly process. The physicochemical characteristics and supercapacitive performance were systematically analyzed. TAC with a microspherical structure promoted and controlled the growth of LDHs, resulting in a more regular sea urchin-like structure, improved dispersibility, reduced resistance, and increased active sites. NiCo-LDH@TAC600-0 (without KOH activation) as an electrode material delivered a specific capacitance (C_s) of 1250 F g^{-1} at 1 A g^{-1} and 1035 F g^{-1} at 10 A g^{-1} , with a rate performance of 82.8%. The asymmetric supercapacitor device using NiCo-LDH@TAC600-0 and TAC provided an energy density of 30.8 Wh kg^{-1} at 800 W kg^{-1} and a capacitance retention rate of 72.5% after 5000 cycles. This study offers a novel approach to enhancing NiCo-LDH properties for efficient energy storage.

Keywords Tannin · Porous carbon · Carbon microspheres · Layered double hydroxides · Supercapacitor · Electrochemical performance

1 Introduction

The increasing global demand for energy and heavy reliance on non-renewable resources pose significant challenges for sustainable development. To address this, research is advancing in diverse energy storage and conversion technologies [1–5]. These technologies not only offer alternative approaches

for energy generation but also hold promise for integration into various environmental applications [6, 7]. However, challenges remain in enhancing efficiency, scalability, and cost-effectiveness. Therefore, new sources of energy such as solar and wind power need to be explored and optimized in order to address this looming energy crisis [8, 9]. However, it needs to be pointed out that the biggest hurdle in the utilization and development of renewable energy sources is the lack of continuity and reliability in their supply, which is dependent on climatic and geographical conditions [10]. Thus, the development of efficient energy storage devices is perhaps one of the most effective strategies that can be adopted to circumvent this problem. Currently, electrochemical energy storage devices are viewed as the most effective and practically feasible energy storage devices and are extensively used for various applications [11]. Traditional energy storage technologies often struggle with limitations such as low power density and limited cycle life, which hinder their application in modern energy systems. Therefore, supercapacitors (SCs) have attracted significant attention from the scientific community due to their high charging/discharging efficiency, excellent power density (Pd), and extended life cycles [12, 13].

✉ Zhanhui Yuan
zhanhuiyuan@fafu.edu.cn

Guanben Du
gongben9@hotmail.com

Haili Gao
haili_gao@fafu.edu.cn

¹ College of Material Engineering, Fujian Agriculture and Forestry University, 63 Xiyuangong Road, Fuzhou 350002, People's Republic of China

² College of Material Science and Engineering, Southwest Forestry University, 300 Bailongsi, Kunming 650224, People's Republic of China

³ College of Engineering, Design and Physical Sciences, Brunel University, Uxbridge, London UB8 3PH, UK

Supercapacitors are broadly classified into electric double-layered capacitors and pseudocapacitors [14–18]. The former class of SCs mostly employs carbon-derived materials for the construction of its electrodes [19], such as graphite, carbon nanotubes, activated carbon, and carbon fibers. Such materials utilize their surface and hierarchical structure to physically adsorb electrolytic ions for energy storage applications and usually provide high life cycles and large power densities. However, the theoretical capacitance and energy density (E_d) values offered by these materials are relatively low [20–23], far from meeting the requirements of future energy systems. In comparison to the carbon-based materials, electrode materials that are typically used in pseudocapacitors such as conductive polymers, transition metal oxides, hydroxides, and sulfides exhibit higher E_d and theoretical capacitance values based on the Faraday reaction by storing energy through the redox reaction during the discharging/charging process [24–27]. Layered double hydroxides (LDHs) [28, 29] are comprised of water molecules, positively charged metal layers, and interlayer anions. They offer tunability of their chemical compositions, a high oxidation–reduction capability, as well as strong intercalation and anion exchange abilities. Thus, they are promising contenders to be used as electrode materials. The material NiCo-LDH [30, 31] has been studied extensively owing to its unique structure and high theoretical specific capacitance (C_s). However, its practical implementation for the development of supercapacitive devices has so far been restricted owing to several problems including serious agglomeration, large volume change, and poor conductivity [32]. These factors seriously limit the transport of electrons and diffusion of electrolytic ions in NiCo-LDH. Therefore, NiCo-LDH falls quite short of achieving its theoretical capacity value and exhibits poor cycling stability during practical applications [33]. Previous studies have explored various combinations of NiCo-LDH with high-conducting materials (including polypyrrole nanotubes, carbon nanotubes, MXene, graphene oxide, and porous carbons) [34–38] for the preparation of LDH/carbon composites with excellent values of C_s and cyclic stability, in order to address these concerns. However, the high cost limits the large-scale application of these materials.

Biomass-derived porous carbons (including activated carbons, carbon microspheres, and carbon fibers) that are extracted from wood, bamboo, plant flowers, walnut shells, chicken bone, and lignin hold the greatest potential to be used as an electrode material for SCs. This is due to the fact that not only are they widely sourced, and low in cost but also exhibit a large specific surface area (SSA), excellent porosity, and stable physicochemical properties [39, 40]. Among them, carbon microspheres offer a unique structure. In this regard, carbon microspheres synthesized through the solvothermal technique are particularly interesting, as their highly porous surface contains rich oxygen-containing functional groups, which allows direct attachment of other functional groups or materials onto their surface without

any further modification to obtain high-performance electrode materials [41–43]. Tannin is a biomass derivative and is abundantly found in higher plants. It also has a wide range of other sources and is commercially available at low prices. It is well known that tannin is the most abundant compound obtained from biomass materials after lignin, cellulose and hemicellulose. This substantiates it as a renewable, green, economical, and nontoxic source for obtaining carbon-based microsphere materials. Moreover, it naturally consists of phenolic biomolecules that contain aromatic ring-bearing hydroxyl groups. Thus, this makes tannin a high carbon-containing material, and therefore a highly attractive source for the preparation of carbon-based microsphere materials [44].

In this work, the biomass material areca tannin was utilized as the precursor owing to its natural composition that contains phenolic biomolecules. The porous carbon microspheres were synthesized through hydrothermal carbonization, followed by the KOH activation process. The microwave hydrothermal method that was employed was more unevenly with high efficiency due to the inside-to-outside heating process in comparison to the conventional hydrothermal technique [45]. Therefore, the NiCo-LDH@TAC composite electrode materials were synthesized further, employing the microwave hydrothermal method as well. The porous carbon microspheres can lower the resistance substantially and effectively avoid the reaggregation of NiCo-LDH. This provides a 3D framework with a high number of active sites and stability of the redox reactions. The impact of morphology and porosity of two different tannin-based carbons on the chemical properties, electrochemical performance, microstructure and pore structure of the synthesized composite electrode materials was studied systematically.

2 Experimental section

2.1 Materials

Areca tannin (condensed tannin with a mass fraction = $70 \pm 2.0\%$ and moisture content = 4–5%) was obtained from Xinhua Co., Ltd., whereas KOH (with purity equal to 85%), HCl (with a mass fraction ranging from 36 to 38%), Co (NO_3)₂·6H₂O, Ni (NO_3)₂·6H₂O, ethylene glycol (EG) and urea were sourced from Shanghai Aladdin Biochemical Co., Ltd. Additionally, Ni foam, acetylene black and PVDF were procured from Cyber Electrochemical Materials Network. Furthermore, N-Methyl-2-pyrrolidone (NMP, N-methylpyrrolidone) was acquired from Tianjin Zhiyuan Chemical Reagent Co., Ltd.

2.2 Synthesis of tannin porous carbons

The details of the synthesis process for tannin-based porous carbon (TAC) materials can be found in a previous study

[44]. The mixture of tannin and water was placed in a microwave hydrothermal reactor to obtain hydrothermal carbon (MHTC). Thereafter, the prepared MHTC sample was mixed with KOH for activation at a temperature of 600 °C with an alkali/carbon (KOH/MHTC) mass ratio equal to 2 (denoted as TAC600-2). The control sample prepared without the addition of any KOH during the pyrolysis process was designated as TAC600-0.

2.3 Preparation of the NiCo-LDH@TAC composite electrode material

Firstly, 1-mmol mixtures of $\text{Co}(\text{NO}_3)_2 \cdot 6\text{H}_2\text{O}$ and $\text{Ni}(\text{NO}_3)_2 \cdot 6\text{H}_2\text{O}$ were added to a 60-mL aqueous solution containing 30% EG, which was then stirred vigorously for 5 min. Thereafter, 0.035 g of the TAC powder was added and then stirred for another 5 min. Finally, 1.5 g of urea was introduced as the precipitation agent, and the prepared solution was poured into a 100-mL hydrothermal synthesis reaction kettle followed by 50 min of intense stirring. The microwave hydrothermal reaction (XH-800S, Beijing Xianghu Co., Ltd, China) was carried out at a temperature of 120 °C for 30 min. The prepared composite material was taken out after completion of the reaction and centrifuged at 8000 rev/min for 5 min to separate out the obtained material from the solvent. The obtained material was then washed with 30% EG aqueous solution multiple times and dried within a vacuum oven for 12 h at 65 °C. The prepared materials were designated as NiCo-LDH@TAC600-0 and NiCo-LDH@TAC600-2 based on the TAC samples that were used. The pure control sample that was synthesized under the same test conditions was denoted as NiCo-LDH (Fig. 1).

2.4 Materials characterization

The structure and surface morphology of the materials were studied via a Hitachi S3400 scanning electron microscope (SEM), as well as a JEM-2100 high-resolution transmission electron microscope (HRTEM) from JEOL, operating at 200 kV. An AXIS Ultra X-ray photoelectron spectrometer (XPS) was employed to determine the chemical composition of the obtained specimens. A Bruker X-ray powder diffractometer (XRD) with Bragg–Brentano geometry was employed to investigate the planar structure of the materials. The specific surface area (S_{BET}), total pore volume ($V_{0.99}$), micropore volume (V_{micro}), and mesopore volume (V_{meso}) values were determined through the N_2 desorption/adsorption analysis [31, 36, 44].

2.5 Electrochemical characterization

The NiCo-LDH@TAC sample, PVDF and acetylene black were added together with a mass ratio equal to 8:1:1 and then granulated in an agate mortar for 5 min till an even distribution was achieved. Thereafter, an appropriate quantity of NMP was added and the resultant mixture was ground for an additional 5 min to form a uniform slurry. The obtained slurry was then evenly spread onto the Ni foam support (with dimensions of 1 cm × 2 cm) and finally dried within a vacuum oven for 12 h at 85 °C to prepare a working electrode for electrochemical testing. A 3-electrode system was then assembled using a working electrode, a saturated calomel utilized as the reference electrode, and a Pt-sheet acting as the counter electrode in a 6 M solution of KOH. The cyclic voltammetry (CV) plots were then obtained within a voltage range spanning from 0 to 0.55 V at ambient temperature, using a Zennium electrochemical workstation from Zahner.

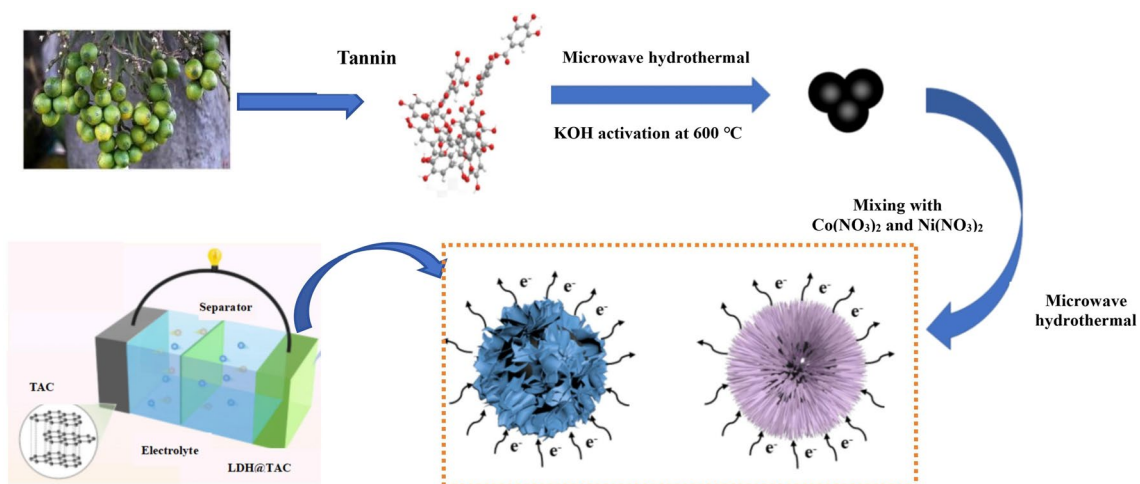


Fig. 1 Schematic diagram illustrating the synthesis scheme employed for the preparation of NiCo-LDH@TAC materials

Additionally, constant current discharge/charge (GCD) plots were obtained in a voltage range from 0 to 0.5 V, whereas electrochemical impedance spectroscopy (EIS) readings were obtained in the frequency window spanning from 10 mHz to 100 kHz. These results were then analyzed to determine the electrochemical characteristics of the synthesized composites. The value of C_s was calculated from the data provided by the GCD measurements using the following mathematical relationship:

$$C_s = (I \times \Delta t) / (m \times \Delta V) \quad (1)$$

where I (A) denotes the discharge current, m (g) refers to the mass of the active substance, ΔV (V) corresponds to the voltage window and Δt (s) refers to the discharge time.

The NiCo-LDH@TACS electrode was utilized as the positive electrode, whereas the TAC electrode acted as the negative electrode. The asymmetric supercapacitor (ASC) was assembled in a 6 M solution of KOH. Electrochemical tests were then performed on this prepared supercapacitive device. The cathode-to-anode mass ratio was obtained using the following relationships:

$$q_+ = q_- \quad (2)$$

$$q = mC\Delta V \quad (3)$$

$$m_+ / m_- = C\Delta V_- / C\Delta V_+ \quad (4)$$

The variables marked with the '+' symbol refer to parameters associated with the positive electrode material whereas the '-' symbol corresponds to the negative electrode. The values of E_d and P_d for the samples were evaluated by employing the following formulae:

$$E_d = (C \times V^2) / 7.2 \quad (5)$$

$$P_d = (E_d \times 3600) / \Delta t \quad (6)$$

3 Results and discussion

3.1 Analysis of morphological, chemical and structural characteristics

The microstructures of the synthesized samples were characterized using SEM. The captured images are provided in Fig. 2a–h. Even though the porous carbon was acquired as a carbon unit consisting of stacked microspheres through microwave-assisted hydrothermal treatment and subsequent pyrolysis process without KOH addition, it still exhibited a somewhat smooth surface, quite similar to other biomass-based hydrothermal carbon materials, as

shown in Fig. 2a [41, 43]. However, KOH activation treatment (refer to Fig. 2b) resulted in increased roughness on the surface of the TAC600-2 sample and multiple pore structures started to appear while completely breaking the microsphere structures. It is clearly shown in Fig. 2c and d that the NiCo-LDH sample that was prepared via the microwave-hydrothermal method was composed of spherical structures formed by densely stacked nanosheets and nanorods. The NiCo-LDH@TAC600-0 sample displayed a more regular spherical structure, as depicted in Fig. 2e. More importantly, as the nanoneedle-like LDH that was anchored onto the carbon microspheres of the TAC600-0 sample (see Fig. 2f), it resulted in a structure that appeared similar to that of a sea urchin, which has a more flexible structure. This special composite structure efficiently prevented the aggregation of the nanoparticles, thereby effectively mitigating the structural degeneration issue. In addition, this structure provided more active sites, which substantially reduced the charge transfer resistance (R_{ct}). It also led to improvement in the capacitance and rate performances (RPs) of the prepared materials [31]. The microscopic structures of the NiCo-LDH@TAC600-2 sample are shown in Fig. 2g and h. The LDH-coated activated carbon sample of TAC600-2 exhibited a higher number of folded and curved sheet structures with a very small number of irregular spherical structures, as can be seen in the figures. It can clearly be observed that the LDH had successfully been anchored onto this irregular carbon TAC600-2 sample. It can be deduced from the results that part of the LDH must have extended into the pore structure, thus inhibiting the formation of LDH microspheres. A large number of irregular composite structures and thick nanosheets lead to obvious stacking, which is not conducive to the exposure of active sites and the electron transport mechanism. It negatively impacts the electrochemical efficiency of the material. The acquired TEM images for the NiCo-LDH@TAC600-0 composite are shown in Fig. 2i–l, which provide further evidence that LDH forms a regular sea urchin-like structure with TAC600-0 carbon microspheres acting as the core. The scanned HRTEM image for the NiCo-LDH@TAC600-0 composite is provided in Fig. 2k, from which the average lattice spacing between the (003) crystal planes was observed to be 0.79 nm [46]. The selected electron diffraction (SAED) image is provided in Fig. 2i. Diffraction rings representing the (003) and (101) crystal planes of NiCo-LDH are clearly shown in the figure, which indicates that the prepared LDH had a polycrystalline structure [47]. The measured TEM–EDX spectra for the NiCo-LDH@TAC600-0 sample revealed that there were five main elements (O, C, Ni, N and Co) present in the composite material and that all the elements were distributed uniformly throughout the sample.

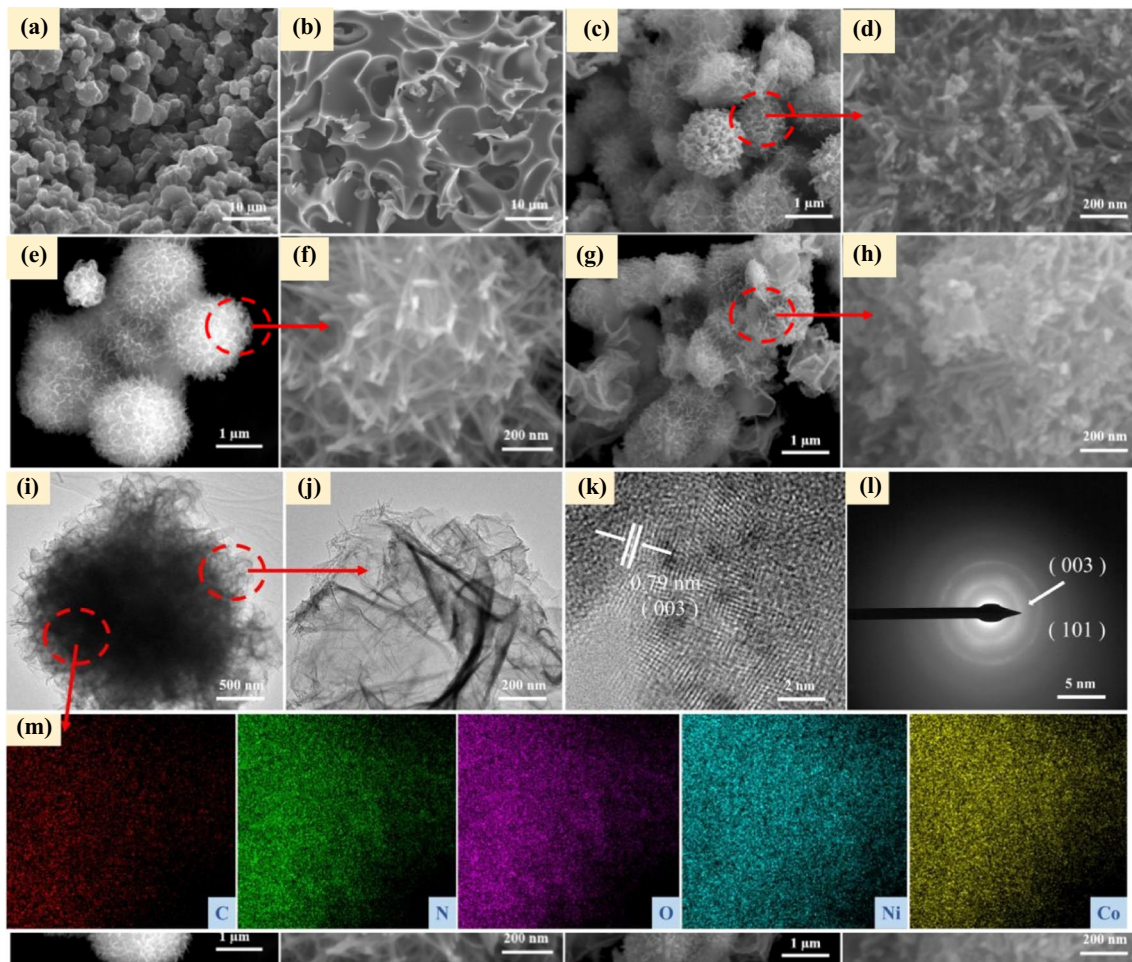


Fig. 2 Morphologies of (a) TAC₆₀₀₋₀, (b) TAC₆₀₀₋₂, (c–d) NiCo-LDH, (e–f) NiCo-LDH@TAC₆₀₀₋₀, and (g–h) NiCo-LDH@TAC₆₀₀₋₂. (i–j) The obtained TEM, (k) SAED, and (l) HRTEM images for the NiCo-LDH@ACF-120 material. (m) The acquired EDS spectra for

the NiCo-LDH@TAC₆₀₀₋₀ sample with the following color codes for the different elements it contained: C (red), N (green), O (purple), Ni (blue), and Co (yellow)

The nitrogen desorption/adsorption isotherms (see Fig. 3a) along with the pore size distribution data (see Fig. 3b) revealed that both the TAC₆₀₀₋₀ and TAC₆₀₀₋₂ samples were mainly composed of micropores. However, the micropores in these samples increased significantly as a result of KOH activation, which is also quite consistent with the SEM results. The obtained PSD curves provided in Fig. 3b confirmed that all the pores were less than 1.5 nm in size for both samples. Furthermore, pore structures of the NiCo-LDH and NiCo-LDH@TAC composites were examined and the obtained results are provided in Fig. 3c and d. All isotherms in Fig. 3c corresponded to the typical type IV with H3-type hysteresis loops in accordance with the IUPAC classification, which indicated that all the materials were primarily mesoporous. The pore size in all three materials including NiCo-LDH, NiCo-LDH@TAC₆₀₀₋₀, and NiCo-LDH@TAC₆₀₀₋₂ predominantly ranged from 1 to 100 nm, as demonstrated by the PSD curves in Fig. 3b.

This observation was consistent with the findings presented in Fig. 3a. The values of SSA and pore volume for the TAC₆₀₀₋₀ sample were found as 453.69 m² g⁻¹ and 0.23 cm³ g⁻¹, respectively. These values increased to 733 m² g⁻¹ and 0.35 cm³ g⁻¹, respectively, for the TAC₆₀₀₋₂ sample with KOH activation. A summary of these texture parameters is provided in Table 1. The SSA values for the samples NiCo-LDH, NiCo-LDH@TAC₆₀₀₋₀, and NiCo-LDH@TAC₆₀₀₋₂ were quite close to each other, with values equal to 51, 56 and 51 m² g⁻¹, respectively. This observation in combination with the microscopic morphology results for the NiCo-LDH, and NiCo-LDH@TAC composites (see Fig. 1) confirmed that the rod, needle, or sheet structure of the nanostructure had coated the microspheres and carbon fragments of the TAC to form the core during the composite forming process. The pore structure of TAC was blocked as the nano-size LDH grew into it and then spread continuously. Therefore, differences in the value of SSA for the

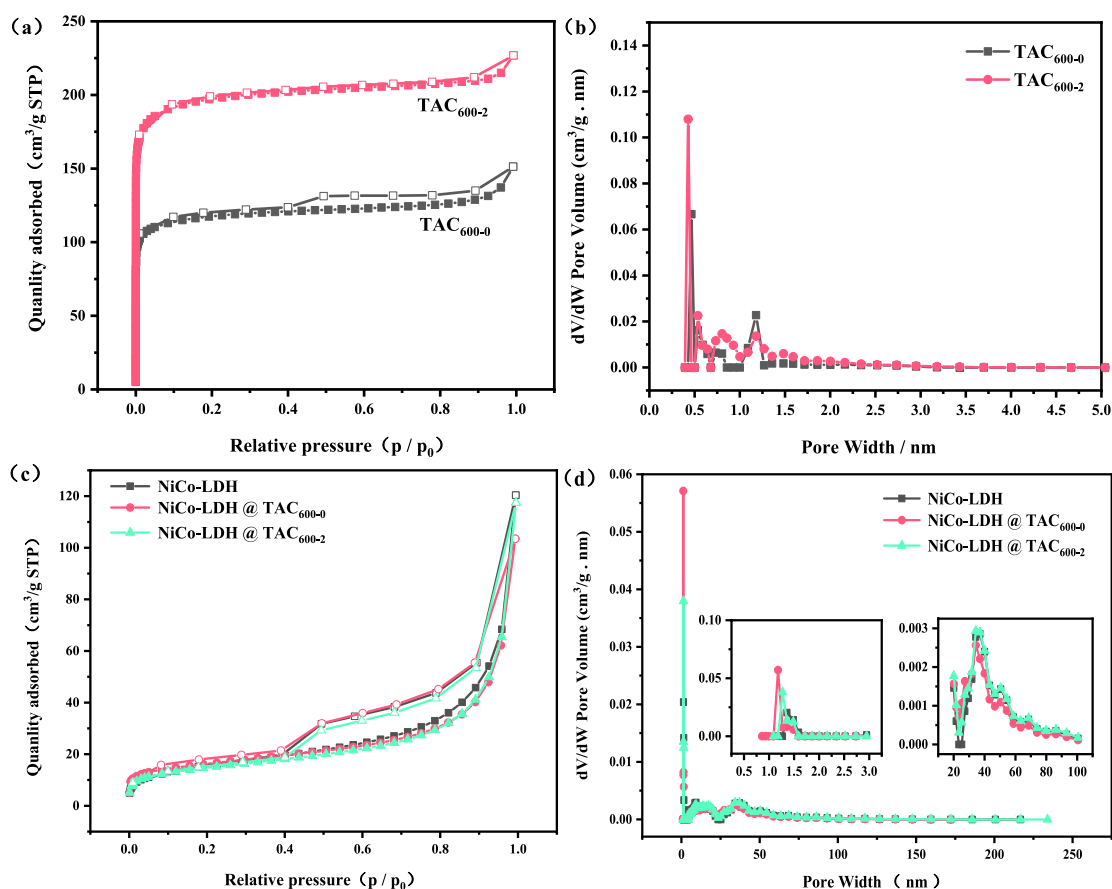


Fig. 3 (a, c) The acquired N₂ desorption/adsorption isotherms and (b, d) PSD curves for the prepared composites

Table 1 Pore structure parameters of LDH and LDH @ TACs

Samples	S_{BET} (m ² g ⁻¹)	$V_{0.99}$ (cm ³ g ⁻¹)	V_{DR} (cm ³ g ⁻¹)	L_0 (nm)	$V_{\text{DR}}/V_{0.99}$	V_{meso} (cm ³ g ⁻¹)
TAC ₆₀₀₋₀	453.69	0.23	0.180	0.87	0.79	0.05
TAC ₆₀₀₋₂	733.00	0.35	0.290	0.68	0.84	0.06
LDH	51.00	0.19	0.019	5.27	0.10	0.17
LDH@TAC ₆₀₀₋₀	56.00	0.16	0.020	1.71	0.13	0.14
LDH@TAC ₆₀₀₋₂	51.00	0.18	0.018	5.60	0.11	0.16

three materials NiCo-LDH, NiCo-LDH@TAC600-0, and NiCo-LDH@TAC600-2 can only be ascribed to the different morphologies and pore structures of their outer coated LDH. It was the sea urchin-shaped NiCo-LDH@TAC600-0 sample that offered the best structural morphology and the highest number of active sites. Therefore, it offers the greatest potential for achieving high electrochemical performance.

The phase composition and crystal structure of the NiCo-LDH and NiCo-LDH@TAC composites were examined using XRD characterization. All three samples exhibited intense diffraction peaks at 2θ values equal to 12.3°, 24.8°, 33.1° and 59° corresponding to the planar directions of (003), (006), (101) and (110) in the NiCo-LDH

nanosheets, as shown in Fig. 4a [48]. No other peak was observed for either of the samples. The characteristic peaks of porous carbon appearing at 2θ values of 22° and 42° were quite insignificant, which suggested that the surface of the NiCo-LDH@TAC composite was constituted of almost pure NiCo-LDH. It proved that the nanoleaflets and nanorod metal hydroxides formed a fully coated structure with TAC as the core to produce a core-shell structure, which was also consistent with the SEM and pore texture results.

Furthermore, FTIR tests were performed on all samples in order to determine the functional groups present at their surfaces. The results of this characterization are presented in Fig. 4b. The figure clearly shows that characteristic peaks

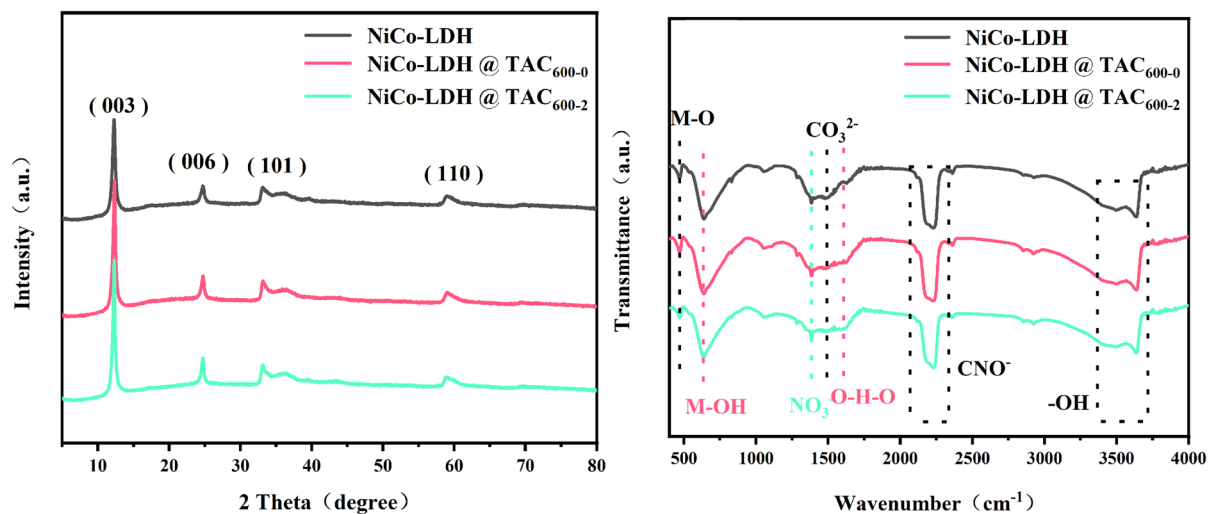


Fig. 4 (a) The acquired XRD and (b) FTIR spectra for the NiCo-LDH, and NiCo-LDH@TAC samples

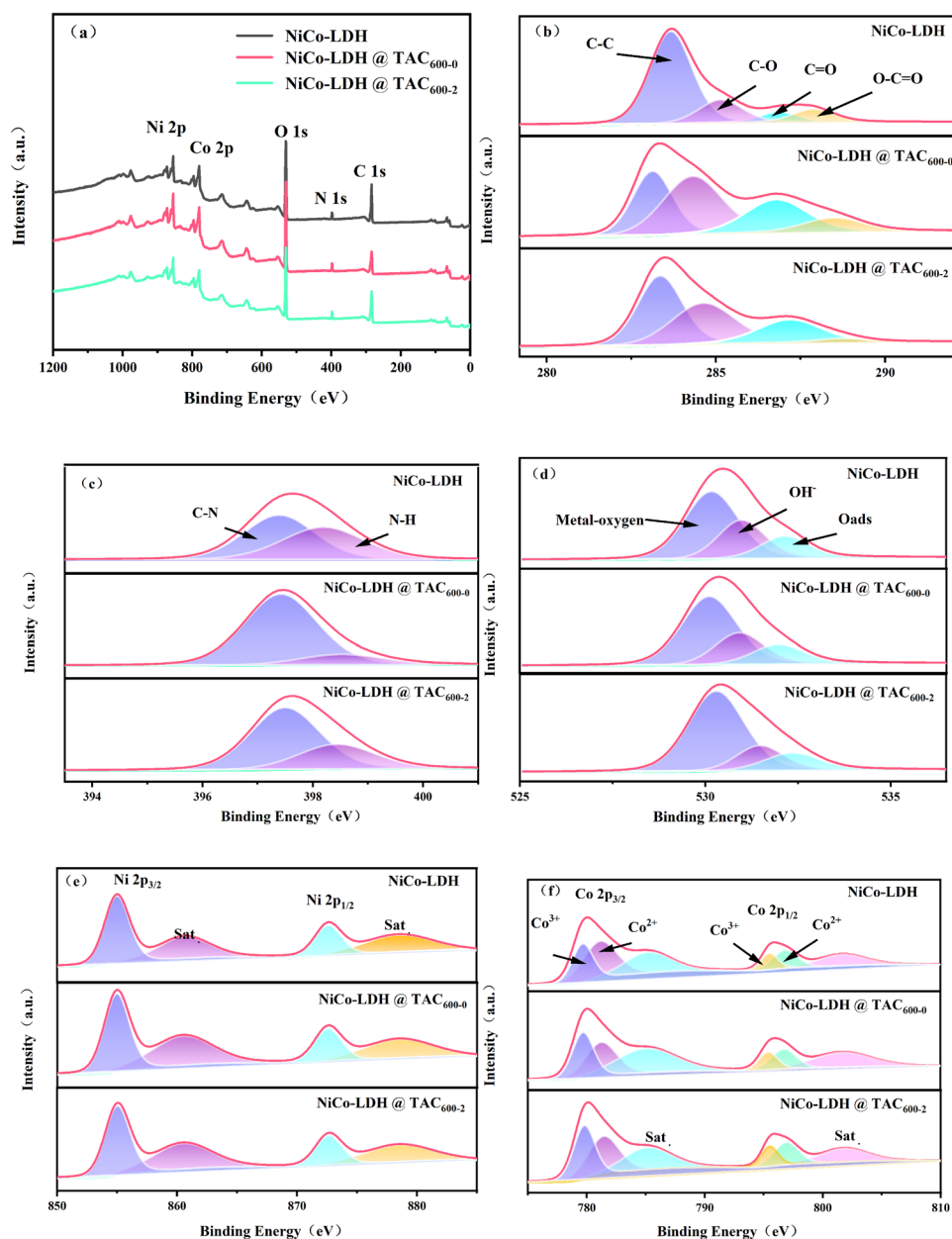
Table 2 Element content of LDH and LDH@TACs

Samples	C (%)	O (%)	N (%)	Ni (%)	Co (%)
NiCo-LDH	45.52	36.31	4.57	6.34	7.26
LDH@TAC600-0	34.40	41.98	5.30	9.71	8.60
LDH@TAC600-2	43.55	36.47	5.26	8.15	6.57

of all samples remained consistent and appeared at the same wavenumber values. This confirmed the successful formation of the core-shell structure and the encapsulation of TAC by LDH. The corresponding elemental percentage compositions are given in Table 2. These results matched well with the SEM and XRD analyses. The two peaks appearing at 465 and 521 cm^{-1} in the spectra of the NiCo-LDH and NiCo-LDH@TAC samples corresponded to the stretching vibrations of the Ni-O and Co-O bonds as well as the stretching vibrations of the bonds Ni-OH and Co-OH. This verified the successful preparation of the LDH material through the microwave hydrothermal method. The small peak observed at 1384 cm^{-1} was associated to the NO_3^- vibrations. The peak found at 1610 cm^{-1} can be linked to the water molecules contained within the microstructure of the material, whereas the small peak appearing at 1485 cm^{-1} , and the strong absorption band appearing at 2241 cm^{-1} corresponded to the interlayer anion CO_3^{2-} and CNO species of LDH, respectively [49–51]. The appearance of CNO can be attributed to the incomplete decomposition of the added precipitant urea [52]. The peaks found at 3498.8 and 3636.7 cm^{-1} were associated to the -OH stretching vibrations, which in turn were also primarily linked to the moisture attached to the surface of the prepared material [53]. These observations together with

the XRD results indicated that the NiCo-LDH and the NiCo-LDH@TAC composites were prepared successfully employing the microwave hydrothermal method and that the CO_3^{2-} and NO_3^- ions were embedded into the metal layer. The elemental composition of the material surface as well as the chemical states were further analyzed using XPS characterization. The XPS spectra acquired for all samples are presented in Fig. 5. The full XPS spectrum is provided in Fig. 5a. The elemental analysis further indicated traces of the Ni, Co, O, C, and N elements in the obtained samples, consistent with the TEM mapping analysis based on Fig. 2. The high-resolution (HR) spectrum of C 1s (refer to Fig. 5b) revealed four peaks located at 283.8 eV, 285.3 eV, 287.0 eV and 288.1 eV and were associated to the C-C, C-O/C-N, C=O and O-C=O bonds [54], respectively. The peaks were fitted using Gaussian functions. The peak observed at 397.4 eV in the HR spectrum of N 1s (see Fig. 5c) was ascribed with the C-N bond, whereas the peak found at 398.8 eV was associated to the N-H bond [55]. Three peaks at 530.2 eV, 531.0 eV and 532.2 eV were found in the HR spectrum of O 1s, as shown in Fig. 5d. They were attributed to metal oxides [56] (such as Ni-O and Co-O), the OH- bond, and chemically adsorbed oxygen [57], respectively. The HR XPS spectrum for Ni 2p was fitted using two spin-orbital and two vibrational satellite peaks (labeled “Sat.”), as depicted in Fig. 5e. The two prominent peaks observed at 855 eV and 872.6 eV had a spin energy difference equal to 17.6 eV and were associated to the Ni 2p_{3/2} and Ni 2p_{1/2} orbitals, respectively. This result was indicative of the spin-orbital characteristics of Ni^{2+} ions in NiCo-LDH. Two vibrational satellite peaks were found at 878.5 and 860.6 eV, which provided further evidence of the presence of Ni^{2+} ions within the NiCo-LDH nanosheets. The HR spectrum of Co 2p (refer to Fig. 5f) confirmed the

Fig. 5 (a) The acquired XPS full survey spectra. The measured XPS spectra for the (b) C 1 s, (c) N 1 s, (d) O 1 s, (e) Ni 2p, and the (f) Co 2p orbitals



presence of two satellite peaks (785.1 eV and 801.6 eV) and two spin-orbital peaks that were observed at 780.9 (Co 2p_{3/2}) and 796.3 eV (Co 2p_{1/2}). The low intensity of the two satellite peaks suggested the coexistence of Co²⁺ and Co³⁺ ions within NiCo-LDH. The peaks appearing at 796.7 and 781.2 eV were associated to the Co²⁺ ions, whereas the peaks observed at 795.4 and 779.1 eV were associated to the Co³⁺ ions [58].

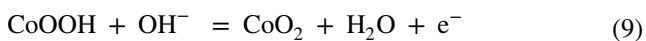
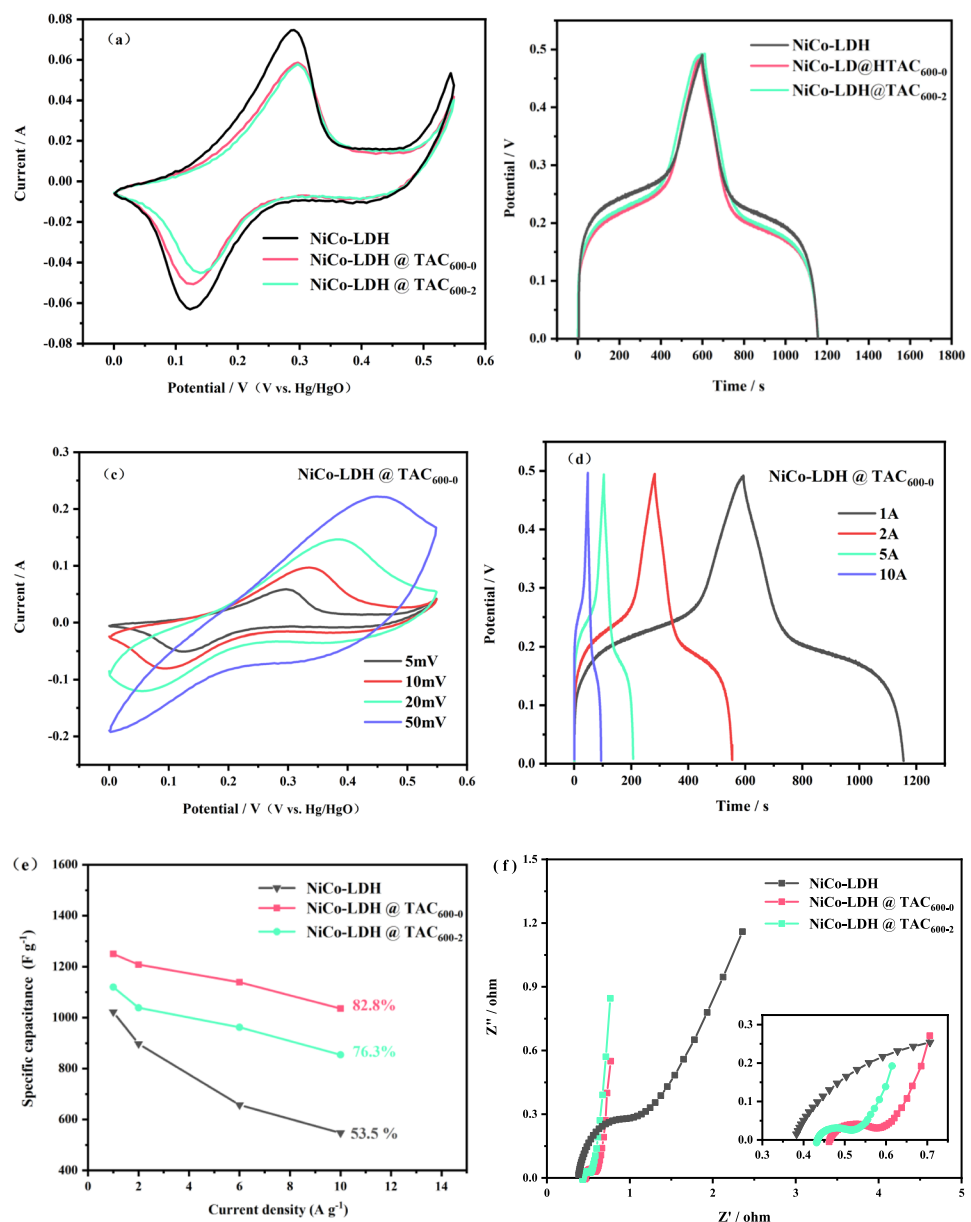
3.2 Electrochemical performance

The electrochemical properties of the obtained materials were analyzed through GCD, EIS and CV measurements

using a 3-electrode configuration in a 6 M electrolytic solution of KOH. The CV plots for the pure NiCo-LDH, as well as both the NiCo-LDH@TAC composite specimens, were acquired at a scan rate (ν) of 5 mV s⁻¹ and are provided in Fig. 6a. A distinct pair of redox peaks appeared for all samples in the voltage window spanning from 0 to 0.55 V. This suggested that the capacitive contribution of the NiCo-LDH@TAC composite electrode mostly came from Faraday pseudocapacitance. The pseudocapacitive behavior can be attributed to the following reactions [31, 49]:



Fig. 6 (a) The acquired CV plots for the pure NiCo-LDH electrode, and both of the NiCo-LDH@TAC composites electrodes at 5 mV s^{-1} . (b) The obtained GCD plots for the pure NiCo-LDH electrode, as well as both of the NiCo-LDH@TAC composite electrodes at $I_d = 1 \text{ A g}^{-1}$. (c) The measured CV plots for the NiCo-LDH@TAC₆₀₀₋₀ electrode at various values of v . (d) The acquired GCD plots for the NiCo-LDH@TAC₆₀₀₋₀ electrodes at different I_d values. (e) A comparison of the plots displaying the variation in C_s with an increase in the value of I_d for the pure NiCo-LDH electrode, and both of the NiCo-LDH@TAC composite electrodes. (f) The measured EIS curves for the pure NiCo-LDH electrode, as well as both of the NiCo-LDH@TAC electrodes



It should be noted that the CV plots of all NiCo-LDH@TAC samples exhibited a smaller gap between the reduction and the oxidation in comparison to the pure NiCo-LDH sample, which indicated better reversibility of the redox reactions for the prepared composite [59]. Almost all of the GCD plots provided in Fig. 6b maintained high symmetry at a current density (I_d) of 1 A g^{-1} . The NiCo-LDH@TAC600-0 sample provided the highest value of C_s equal to 1250 F g^{-1} , followed by NiCo-LDH@TAC600-2 and NiCo-LDH with values of 1120 and 1022 F g^{-1} , respectively.

Interestingly, the pores of TAC were mostly concentrated in the micropores following KOH activation treatment according to a previous study, where the pore size distribution moved to the higher end with an increase in the number of micropores. The micropores offer a larger contact area and thus lead to the availability of more active sites within the material. This also enhances the wettability of the material, as the mesopores provide a faster diffusion tube for the electrolytic ions [60]. It must be noted that the value of C_s for the NiCo-LDH@TAC samples was found to be negatively correlated with the porosity of the porous carbons. This implied that the properties exhibited by the resulting composite were not just a simple combination of individual advantages of its constituents, but were dependent on the new composite structure that was formed. The structure of

TAC was primarily composed of relatively regular carbon microspheres for the composite TAC600-0 that was prepared without KOH activation treatment, and the composite exhibited a spherical structure formed by nanosheets and nanorod-like LDH-coated carbon microspheres. Such a structure can provide a higher number of active sites and a larger electrolyte/electrode contact area [31]. Also, the porous carbon microspheres present inside can provide improved and stable support to form an excellent urchin-like core-shell structure. Therefore, the NiCo-LDH@TAC600-0 electrode offered the best C_s and RP values. For the TAC sample with KOH activation treatment, the microspherical structure was disintegrated into smaller carbon fragments. Thus, the nano-size LDH structure in this case grew into the pores of the carbon material during the combination process, owing to the irregularity of the carbon sheet and the rich pore structure on the surface. This led to an irregular coating structure, coils and agglomerations, which resulted in a low number of reaction sites for the electrode and thus low electrochemical efficiency. The CV plots for the NiCo-LDH@TAC600-0 electrode obtained at values of ν spanning from 5 to 50 mV s^{-1} are provided in Fig. 6c. Apparently, the reduction and oxidation peaks gradually moved towards negative and positive potentials, respectively, as the value of ν was increased. This can be associated to charge diffusion polarization. However, the shape of the CV curve was preserved and the oxidation and the reduction peaks did not completely disappear, indicating that the prepared electrode offered an excellent value of RP. The GCD plots of the NiCo-LDH@TAC600-0 electrode in the I_d range spanning from 1 to 10 A g^{-1} are provided in Fig. 6d. All curves exhibited good symmetry, which implied that the composite electrode was highly suitable for reversible redox reactions and delivered high Coulomb efficiency during the discharge/charge cycle. Furthermore, the values of C_s for the obtained samples were calculated from the GCD plots obtained for the NiCo-LDH and NiCo-LDH@TAC electrodes at different values of I_d in order to gain a more intuitive assessment of the improvement in the RP of NiCo-LDH after the introduction of TAC. The obtained results are presented in Fig. 6e. The maximum RP of the NiCo-LDH@TAC600-0 electrode (82.8%) was clearly much higher in comparison to the value that was obtained for the NiCo-LDH (53.5%) electrode prepared under the same conditions. It was also either comparable to or higher than the values achieved in prior studies [31, 49, 55, 59, 61]. This excellent performance highlights the synergistic advantage of using a sea urchin-like core-shell of NiCo-LDH with a 3D-graded porous carbon TAC acting as the support substrate. Additionally, the charge transfer dynamics and conductivity of all electrodes were also investigated using EIS, the results of which are presented in Fig. 6f. The obtained Nyquist plot consisted of a semicircle curve in the high-frequency (HF) regime and a straight-line

graph in the low-frequency (LF) regime. The intercept in the HF regime denotes the series resistance (R_s), whereas the diameter of the small semicircle gives the value of R_{ct} . The slope of the linear plot in the LF regime corresponds to the diffusion resistance (R_d) [62]. As shown in Fig. 6f, the curve obtained for the electrode of the NiCo-LDH@TAC samples was nearly vertical in the LF regime, indicating an extremely low value of R_d . All electrodes exhibited low series resistances, which were much lower compared to the values reported in previous studies on NiCo-LDH [47, 50–53]. The values of R_{ct} and R_d for all composite electrodes were found to be smaller in comparison to the pure NiCo-LDH electrode. This can be ascribed to the rapid transfer path of electrolytic ions provided by the 3D porous carbon with a highly porous structure.

3.3 Electrochemical properties of the ASC devices

The efficiency and performance of the electrodes were evaluated for practical applications by assembling ASC devices using a 6 M solution of KOH as the electrolyte, with NiCo-LDH@TAC600-0 acting as the positive electrode and TAC600-2 taken as the negative electrode (the mass load ratio of the two electrodes was calculated using Eq. (4)). The highest stable operating voltage of the assembled ASC device was determined by conducting CV and GCD tests on the device at different voltage ranges. The CV tests were conducted at $\nu = 5 \text{ mV s}^{-1}$, whereas the GCD readings were taken at an I_d value equal to 1 A g^{-1} . The results of these characterizations are provided in Fig. 7a and b, respectively. The obtained CV curve clearly showed an absence of any significant polarization as the voltage reached a value of 1.6 V. Furthermore, the charging phase of the GCD curve did not exhibit a pronounced slow increase, while also maintaining high symmetry. This confirmed the stability of the prepared ASC devices at a voltage equal to 1.6 V. The CV plots of the prepared device that were taken at various ν values ranging from 5 to 100 mV s^{-1} at 1.6 V are presented in Fig. 7c. Distinct redox peaks corresponding to the Faraday pseudocapacitance of the NiCo-LDH@TAC600-0 electrode were clearly observed in the figure. It must be noted that all the CV curves exhibited similar shapes and did not experience heavy distortion even at a high ν value equal to 100 mV s^{-1} . This clearly suggested that the prepared ASC device provided exceptional reversibility and RP values [63]. In addition, GCD curves of the ASC devices that were acquired at different values of I_d are presented in Fig. 7d. It can clearly be seen that all these curves are symmetric and no obvious drop in voltage (iR) had occurred. This indicated a low value of R_s and good electrochemical reversibility of the ASC devices [64]. The values of E_d and P_d for the devices were determined by employing Eq. (5) and Eq. (6), respectively. The corresponding Ragone plot is provided in

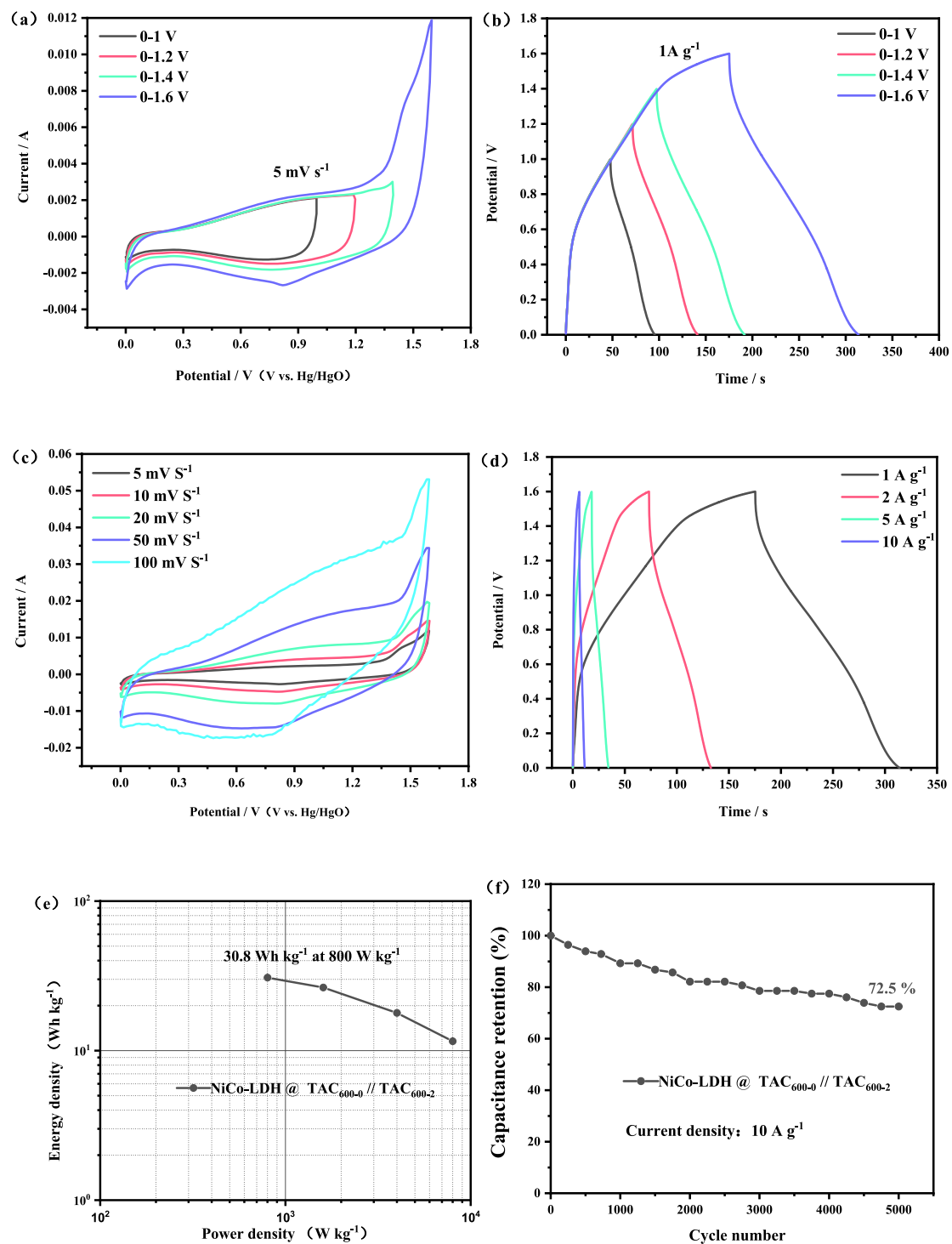


Fig. 7 The obtained performance parameters for the assembled NiCo-LDH@TAC₆₀₀₋₀//TAC₆₀₀₋₄ ASC. **(a)** The measured CV plots for various potential ranges at $\nu = 5 \text{ mV s}^{-1}$. **(b)** The acquired GCD plots for various windows of potentials at $I_d = 0.5 \text{ A g}^{-1}$. **(c)** The obtained CV

plots at different ν values. **(d)** The measured GCD plots at different I_d values. **(e)** The Ragone diagram and **(f)** results for the cycling stability of the assembled ASC devices

Fig. 7e. The NiCo-LDH@TAC600-0//TAC ASC exhibited a maximum E_d value of 30.8 Wh kg^{-1} at $P_d = 800 \text{ W kg}^{-1}$. The obtained E_d and P_d values were comparable or higher in

comparison to their values for NiCo-LDH reported in previous studies (as summarized in Table 3). The long-term cycle stability data for the ASC device, obtained from the constant

Table 3 The performance of the supercapacitors obtained in this work is compared with similar devices reported in the literature

Material	Energy density (Wh kg ⁻¹)	Power density (W kg ⁻¹)	Cyclic stability (%)	Reference
NCNRs@NCNSs	22.8	375	90.85/5000 cycles	[61]
ZnCo ₂ O ₄ /NiCo-LDH//AC	44.5	800	71.5/5000 cycles	[56]
NiCo LDH/ IPC//IPC	29.6	744	88/4000 cycles	[64]
NF@F-NCCH12// AC	35.3	375	91.6/10000 cycles	[65]
Co _{0.75} Ni _{0.25} (OH) ₂ : D//AC	26.7	800	75/1000 cycles	[66]
NCPS@C@G//AC	33.2	800	87.1/1000 cycles	[67]
NiCo-LDH-S/PNTs// GF-LDH	16.3	650	75/8000 cycles	[68]
NiCo-LDH@rGO//AC	32.2	236	80.4/10000 cycles	[69]
NiCo-LDH @ TAC ₆₀₀₋₀ //TAC ₆₀₀₋₄	30.8	800	72.5/5000 cycles	This work

current discharge/charge test at $I_d = 10 \text{ A g}^{-1}$ after completing 5000 cycles is presented in Fig. 7f. The results showed that the ASC device managed to achieve a capacitance retention value of 72.5% even after completing 5000 cycles at a high I_d value of 10 A g^{-1} . Additionally, the NiCo-LDH@TAC600-0 electrode prepared in this work exhibited a higher value of E_d along with excellent cycling stability in comparison to pure or modified NiCo-LDH electrodes reported by other studies (see Table 2). In general, the NiCo-LDH@TAC600-0 electrode material prepared by the microwave hydrothermal method provided a high C_s value, excellent RP, and impressive cycling stability for the assembled ASC devices. A schematic diagram illustrating the preparation process and mechanism is provided in Fig. 1. The carbon microspheres provided good support for the LDH material, resulting in the high dispersion of NiCo-LDH and a large number of ion channels. The rod- and sheet-shaped nano-LDH was able to form 3D frameworks with regular sea urchin-like spines as the shell and TAC600-0 as the core, as a result of the microwave hydrothermal treatment. This provided a high number of active sites and lent stability to the redox reactions This positively impacted the cycle stability as well as the capacitance and rate performances of the prepared composite electrode.

4 Conclusions

In this study, tannin-based porous carbons with varying microstructures, pore structures, and physicochemical characteristics were developed via a two-step process, including microwave hydrothermal pre-carbonization followed by KOH activation treatment using areca tannin as the precursor. The NiCo-LDH@TAC composites were prepared through a microwave hydrothermal co-assembly process using TAC as the substrate. The results of the study revealed that the morphology and structure of TAC affected the growth of the LDH nanosheets. The relatively smooth carbon microspheres (TAC600-0) enabled and facilitated

LDH to form a 3D interwoven structure with more regular sea urchin-like spines as the shell, while activated porous carbon (TAC600-2) resulted in a more disordered structure, leading to a certain amount of accumulation. The prepared NiCo-LDH@TAC600-0 electrode material exhibited excellent electrochemical performance in the 3-electrode test system with a 6 M solution of KOH employed as the electrolyte. The highest C_s value equal to 1250 F g^{-1} was achieved at $I_d = 1 \text{ A g}^{-1}$, whereas the rate performance for the material reached as high as 82.8%. The ASC device assembled using TAC was able to deliver a high E_d value of 30.8 Wh kg^{-1} (at $P_d = 800 \text{ W kg}^{-1}$), having a capacitance retention rate of 72.5% following 5000 cycles at $I_d = 10 \text{ A g}^{-1}$. Therefore, the findings of this study provide sufficient evidence that it has good application prospects in SC devices. The work also opens pathways to explore innovative ideas along similar lines for mitigating the issues of high agglomeration, large volume change, and poor electrical conductivity of LDH materials.

Acknowledgements The authors thank Shyamji Lab (www.shiyanjia.com) for the assistance in the XPS tests.

Author contributions Weigang Zhao: Conceptualization, Investigation, Methodology, Formal Analysis, Software, Writing—Original Draft, Writing—Review & Editing, Supervision, Project Administration. Jianping Deng and Menghan Li: Conceptualization, Data Curation, Validation, Writing—Original Draft. Haili Gao: Software, Validation. Mizi Fan: Investigation, Writing—Review & Editing. Guanben Du: Resources, Supervision, Writing—Review & Editing. Zhanhui Yuan: Supervision, Conceptualization, Validation, Resources, Writing—Review & Editing.

Funding The authors received financial support for this work from the National Natural Science Foundation of China (Grants 32071688), the central government guides local funds for scientific and technological development (2023L3044), Fujian Agriculture and Forestry University Science and Technology innovation special fund project (Grants KFB23142 and KFB24010), and the Innovative training program for college students of FAFU (Grants 202410389342).

Data availability The data that support the findings of this study are available from the corresponding authors upon reasonable request.

Declarations

Competing interests The authors declare no competing interests.

Open Access This article is licensed under a Creative Commons Attribution-NonCommercial-NoDerivatives 4.0 International License, which permits any non-commercial use, sharing, distribution and reproduction in any medium or format, as long as you give appropriate credit to the original author(s) and the source, provide a link to the Creative Commons licence, and indicate if you modified the licensed material. You do not have permission under this licence to share adapted material derived from this article or parts of it. The images or other third party material in this article are included in the article's Creative Commons licence, unless indicated otherwise in a credit line to the material. If material is not included in the article's Creative Commons licence and your intended use is not permitted by statutory regulation or exceeds the permitted use, you will need to obtain permission directly from the copyright holder. To view a copy of this licence, visit <http://creativecommons.org/licenses/by-nc-nd/4.0/>.

References

- Wu Z, Deng X, Yu X, Gu J, El-Bahy ZM, Mersal GAM et al (2024) Electrospun thermoplastic polyurethane membrane decorated with carbon nanotubes: a platform of flexible strain sensors for human motion monitoring. *Polymer* 303:127120
- Siricharoenpanich A, Poojeera S, Srichat A, Vengsungnle P, Naphon P. Optimized performance of closed loop control electromagnetic field for the electric generators with energy storage. *Engineered Science*. 2024.
- Rebillion H, Henao O, Gutiérrez E, Amell A, Colorado H. Thermoelectric modules: applications and opportunities in building environments for sustainable energy generation: from biomass, municipal waste, and other sources. *Engineered Science*. 2024.
- Dhorkule M, Lamrood P, Ralegankar S, Patole S, Wagh S, Pathan H. Unveiling the efficiency of dye-sensitized solar cells: a journey from synthetic to natural dyes. *ES Food & Agroforestry*. 2024.
- Sigamani S, Dubey RSDORS, G.V.S S. Electrochemically deposited ZnO and Sol-Gel spin-coated Zn-doped TiO₂ thin films on FTO: an optical investigation. *ES Energy & Environments*. 2023;22.
- Yuan Y, Zhang C, Jiang B, Lei Y, Li Z, Sun K et al (2024) A robust photothermal superhydrophobic anti/de-icing composite coating fabricated from BP/SiO₂ on a modified fluorocarbon coating base. *Prog Org Coat* 196:108725
- Shi Y, Liang B, Gao H, Zhao R, Dong Q, Li T et al (2024) Research progress on spherical carbon-based electromagnetic wave absorbing composites. *Carbon* 227:119244
- Braff WA, Mueller JM, Trancik JE (2016) Value of storage technologies for wind and solar energy. *Nat Clim Chang* 6(10):964–969
- Das M. Photovoltaic-battery-supercapacitor water pumping system and its reliability under fluctuating environmental conditions. *ES Energy & Environment*. 2024.
- Yousif M, Ai Q, Wattoo WA, Jiang Z, Hao R, Gao Y (2019) Least cost combinations of solar power, wind power, and energy storage system for powering large-scale grid. *J Power Sources* 412:710–716
- Shan X, Wu J, Zhang X, Wang L, Yang J, Chen Z, et al. Wood for application in electrochemical energy storage devices. *Cell Reports Physical Science*. 2021;2(12).
- Sharma P, Kumar V (2020) Current technology of supercapacitors: a review. *J Electron Mater* 49(6):3520–3532
- Yuan Y, Yang P, Wang Z, He Q, Sun K, Fan R. Epsilon-negative materials with lower percolation threshold derived from segregated structures. *Polymer Composites.n/a(n/a)*.
- Fan W, Wang Q, Rong K, Shi Y, Peng W, Li H et al (2023) MXene enhanced 3D needled waste denim felt for high-performance flexible supercapacitors. *Nano-Micro Letters* 16(1):36
- Dahivade P, Randive S, Fugare D, Sathe V, Thakur A, Lokhande B. Nano-crystalline cadmium oxide thin films for supercapacitor application: effect of solution concentrations. *ES Energy & Environment*. 2024.
- V S, G B, Lokhande BJ, Ambare R. Electro-synthesized bismuth oxide nanomaterials on flexible substrate electrode for supercapacitor application. *ES Energy & Environment*. 2023.
- Chanthee S, Asavatesanupap C, Sertphon D, Nakkhong T, Subjalearndee N, Santikunaporn M (2024) Electrospinning with natural rubber and Ni doping for carbon dioxide adsorption and supercapacitor applications. *Engineered Science* 27:975
- Sidheekha MP, Shabeeba A, Rajan L, Thayyil MS, Ismail YA (2023) Conducting polymer/hydrogel hybrid free-standing electrodes for flexible supercapacitors capable of self-sensing working conditions: large-scale fabrication through facile and low-cost route. *Engineered Science* 23:890
- Zhao Y, Qiao W, Wang H, Xie Y, Teng B, Li J et al (2024) Introducing phosphoric acid to fluorinated polyimide towards high performance laser induced graphene electrodes for high energy micro-supercapacitors. *Carbon* 230:119665
- Nithya VD. A review on holey graphene electrode for supercapacitor. *Journal of Energy Storage*. 2021;44.
- Tian N, Gao M, Liu X-H, Liu X, Yang T, Xie W, et al. Activated carbon derived from walnut green peel as an electrode material for high-performance supercapacitors. *Biomass Conversion and Biorefinery*. 2022.
- Fikry M, Abbas M, Sayed A, Nouh A, Ibrahim A, Mansour AS (2022) Using a novel graphene/carbon nanotubes composite for enhancement of the supercapacitor electrode capacitance. *J Mater Sci: Mater Electron* 33(7):3914–3924
- Zhao C, Guo J, Fan J, Zhang X, Zhao C, Chen S. Surface engineering of reclaimed carbon fiber (RCF) electrode for superimposed supercapacitor performance. *Journal of Energy Storage*. 2022;46.
- De Adhikari A, Shauloff N, Turkulets Y, Shalish I, Jelinek R. Tungsten-disulfide/polyaniline high frequency supercapacitors. *Advanced Electronic Materials*. 2021;7(6).
- Li Z, Li J, Wu B, Wei H, Guo H, El-Bahy ZM et al (2024) Interfacial-engineered robust and high performance flexible polylactic acid/polyaniline/MXene electrodes for high-performance supercapacitors. *J Mater Sci Technol* 203:201–210
- Naeem S, Shaikh A, Up S, Patil A. Electrochemical deposition, synthesis, and characterization of dopant-free cobalt hydroxide as an enhanced electrode material for supercapacitors. *ES Energy & Environment*. 2023.
- P.Thokale SP, Mhetre MT, Ranadive SG, Lokh BJ, e e. Impact of sulfuric acid concentration variation in the synthesis of polyaniline and on electrochemical performance of polyaniline thin films prepared at room temperature. *ES Energy & Environment*. 2024;23:1112.
- Li X, Du D, Zhang Y, Xing W, Xue Q, Yan Z (2017) Layered double hydroxides toward high-performance supercapacitors. *Journal of Materials Chemistry A* 5(30):15460–15485
- Mancharkar A, Bodke M, Malavekar D, Bulakhe R, Kim JM, Kim J, et al. Cadmium hydroxide nanowires for high performance supercapacitor by chemical bath deposition. *ES Energy & Environment*. 2023.

30. Shan X, Guo Z, Qu Z, Zou Y, Zhao L, Chen P (2022) Boosting the performance of nickel–cobalt LDH cathode with phosphorus and selenium co-doping for hybrid supercapacitor. *Materials Research Letters* 10(9):593–601
31. Luo L, Wang S, Zhou Y, Yan W, Gao H, Luo L et al (2022) Microwave-assisted synthesis of hybrid supercapacitors consisting of Ni, Co-layered double hydroxide shell assembled around wood-derived activated carbon fiber core. *Electrochim Acta* 412:140148
32. Li Z, Huang Y, Zhang Z, Wang J, Han X, Zhang G et al (2021) Hollow C-LDH/Co₉S₈ nanocages derived from ZIF-67-C for high-performance asymmetric supercapacitors. *J Colloid Interface Sci* 604:340–349
33. Ramachandran R, Lan Y, Xu Z-X, Wang F (2020) Construction of NiCo-layered double hydroxide microspheres from Ni-MOFs for high-performance asymmetric supercapacitors. *ACS Applied Energy Materials* 3(7):6633–6643
34. Zang Y, Luo H, Zhang H, Xue H (2021) Polypyrrole nanotube-interconnected NiCo-LDH nanocages derived by ZIF-67 for supercapacitors. *ACS Applied Energy Materials* 4(2):1189–1198
35. Wang Y, Xu F, Zhou F, Dai L, Qu K, Wu Y et al (2022) Room-temperature synthesis of NiCo-layered double hydroxide/MXene composites for high-performance supercapacitors. *Ind Eng Chem Res* 61(25):8800–8808
36. Zeng J, Xie W, Guo Y, Zhao T, Zhou H, Wang Q et al (2024) Magnetic field facilitated electrocatalytic degradation of tetracycline in wastewater by magnetic porous carbonized phthalonitrile resin. *Appl Catal B* 340:123225
37. Wang C, Liang B, Gao H, Yang T, Li T, Ma Y et al (2024) Efficiently removing four cationic dyes from aqueous solution by magnetite@polypyrrole@2-acrylamido-2-methyl-1-propanesulfonic acid microspheres. *Colloids Surf, A* 700:134659
38. Bakytkarim Y, Tursynbolat S, Mukatayeva Z, Tileuberdi Y, Shadin NA, Assirbayeva ZM, et al. High-sensitivity electrochemical detection of chlorogenic acid based on Pt@r-GO@MWCNTs Ternary nanocomposites modified electrodes. *Engineered Science*. 2024.
39. Sun L, Gong Y, Li D, Pan C (2022) Biomass-derived porous carbon materials: synthesis, designing, and applications for supercapacitors. *Green Chem* 24(10):3864–3894
40. Sankar V, Sundararajan A, Eswaran M, Dhanusuraman D (2024) Hierarchical porous activated carbon derived from *Callistemon viminalis* leaf biochar for supercapacitor and methylene blue removal applications 24:1–15
41. Elmouwahidi A, Bailón-García E, Pérez-Cadenas AF, Celzard A, Fierro V, Carrasco-Marín F (2021) Carbon microspheres with tailored texture and surface chemistry as electrode materials for supercapacitors. *ACS Sustainable Chemistry & Engineering* 9(1):541–551
42. Sanchez-Sanchez A, Izquierdo MT, Mathieu S, González-Álvarez J, Celzard A, Fierro V (2017) Outstanding electrochemical performance of highly N- and O-doped carbons derived from pine tannin. *Green Chem* 19(11):2653–2665
43. Zhou Y, Yan W, Yu X, Chen T, Wang S, Zhao W (2020) Boron and nitrogen co-doped porous carbon for supercapacitors: a comparison between a microwave-assisted and a conventional hydrothermal process. *Journal of Energy Storage* 32:101706
44. Deng J, Zhang Q, Lan Y, Luo L, Dai Z, Lin Z, et al. Two-step preparation of hierarchical porous carbon materials derived from tannin for use as an electrode material for supercapacitors. *Journal of Renewable Materials*. 2023;11(6)
45. Dahivade P, Pawar S, Pathan H, Lokhande B. Temperature-dependent hydrothermal synthesis of CdO nanoparticles and its analysis for supercapacitor application. *ES Energy & Environment*. 2024.
46. Xue X, Zhong J, Liu J, Hou Z, Wu X, Li S, et al. Hydrolysis of metal-organic framework towards three-dimensional nickel cobalt-layered double hydroxide for high performance supercapacitors. *Journal of Energy Storage*. 2020;31
47. Amin KM, Krois K, Muench F, Etzold BJM, Ensinger W (2022) Hierarchical pipe cactus-like Ni/NiCo-LDH core-shell nanotube networks as a self-supported battery-type electrode for supercapacitors with high volumetric energy density. *Journal of Materials Chemistry A* 10(23):12473–12488
48. Hu W, Chen L, Du M, Song Y, Wu Z, Zheng Q. Hierarchical NiCo-layered double hydroxide nanoscroll@PANI nanocomposite for high performance battery-type supercapacitor. *Electrochimica Acta*. 2020;338.
49. Zhang C, Zhang L, Liu Q, Ding Y, Cheng L, Wu M, et al. Enhanced interfacial electron transfer by constructing NiCo-LDH hollow nanocages decorated N-doped graphene quantum dots heterojunction for high-performance supercapacitors. *Applied Surface Science*. 2022;602
50. Zhao X, Li H, Zhang M, Pan W, Luo Z, Sun X (2022) Hierarchical nanocages assembled by NiCo-Layered double hydroxide nanosheets for a high-performance hybrid supercapacitor. *ACS Appl Mater Interfaces* 14(30):34781–34792
51. Su W, Wu F, Fang L, Hu J, Liu L, Guan T et al (2019) NiCo-LDH nanowires@nanosheets core-shell structure grown on carbon fiber cloth for high performance flexible supercapacitor electrode. *J Alloy Compd* 799:15–25
52. Zhao Y, Wang Q, Bian T, Yu H, Fan H, Zhou C et al (2015) Ni³⁺-doped monolayer layered double hydroxide nanosheets as efficient electrodes for supercapacitors. *Nanoscale* 7(16):7168–7173
53. Ouyang Y, Xing T, Chen Y, Zheng L, Peng J, Wu C, et al. Hierarchically structured spherical nickel cobalt layered double hydroxides particles grown on biomass porous carbon as an advanced electrode for high specific energy asymmetric supercapacitor. *Journal of Energy Storage*. 2020;30.
54. Chu D, Li F, Song X, Ma H, Tan L, Pang H et al (2020) A novel dual-tasking hollow cube NiFe₂O₄-NiCo-LDH@rGO hierarchical material for high performance supercapacitor and glucose sensor. *J Colloid Interface Sci* 568:130–138
55. Xiong H, Liu L, Fang L, Wu F, Zhang S, Luo H, et al. 3D self-supporting heterostructure NiCo-LDH/ZnO/CC electrode for flexible high-performance supercapacitor. *Journal of Alloys and Compounds*. 2021;857.
56. Zhu M, Cai W, Wang H, He L, Wang Y. Rational construction of MOF-derived Zn-Co-O/NiCo-LDH core/shell nanosheet arrays on nickel foam for high-performance supercapacitors. *Journal of Alloys and Compounds*. 2021;884.
57. Li M, Cheng JP, Wang J, Liu F, Zhang XB (2016) The growth of nickel-manganese and cobalt-manganese layered double hydroxides on reduced graphene oxide for supercapacitor. *Electrochim Acta* 206:108–115
58. Chen F, Chen C, Hu Q, Xiang B, Song T, Zou X, et al. Synthesis of CuO@CoNi LDH on Cu foam for high-performance supercapacitors. *Chemical Engineering Journal*. 2020;401.
59. Padalkar NS, Sadavar SV, Shinde RB, Patil AS, Patil UM, Dhawale DS et al (2022) Layer-by-layer nanohybrids of Ni-Cr-LDH intercalated with 0D polyoxotungstate for highly efficient hybrid supercapacitor. *J Colloid Interface Sci* 616:548–559
60. Luo L, Lan Y, Zhang Q, Deng J, Luo L, Zeng Q, et al. A review on biomass-derived activated carbon as electrode materials for energy storage supercapacitors. *Journal of Energy Storage*. 2022;55.
61. Zheng K, Liao L, Zhang Y, Tan H, Liu J, Li C et al (2022) Hierarchical NiCo-LDH core/shell homostructural electrodes with MOF-derived shell for electrochemical energy storage. *J Colloid Interface Sci* 619:75–83

62. Wu Z, Wang X, Annamareddy S, Gao S, Xu Q, Algadi H, et al. Dielectric properties and thermal conductivity of polyvinylidene fluoride synergistically enhanced with Silica@Multi-walled carbon nanotubes and boron nitride. *ES Materials & Manufacturing*. 2023.
63. Liao F, Yang G, Cheng Q, Mao L, Zhao X, Chen L. Rational design and facile synthesis of Ni-Co-Fe ternary LDH porous sheets for high-performance aqueous asymmetric supercapacitor. *Electrochimica Acta*. 2022;428.
64. Zhang X, Lu Q, Guo E, Feng J, Wei M, Ma J. NiCo layer double hydroxide/biomass-derived interconnected porous carbon for hybrid supercapacitors. *Journal of Energy Storage*. 2021;38.
65. Qin Y, Du Q, Deng J, Zou J, Lu G, Wang P (2022) Electronic structure modulation and phase transformation of nickel-cobalt carbonate hydroxide caused by halogen doping and its effect on supercapacitor performance. *ACS Applied Energy Materials* 5(1):469–480
66. Xiao B, Zhu W, Li Z, Zhu J, Zhu X, Pezzotti G (2018) Tailoring morphology of cobalt-nickel layered double hydroxide via different surfactants for high-performance supercapacitor. *R Soc Open Sci* 5(9):180867
67. Su S, Sun L, Qian J, Shi X, Zhang Y (2021) Hollow bimetallic phosphosulfide NiCo-P/S nanoparticles in a CNT/rGO framework with interface charge redistribution for battery-type supercapacitors. *ACS Applied Energy Materials* 5(1):685–696
68. Wu YF, Hsiao YC, Liao CH, Hsu CS, Yougbare S, Lin LY (2022) Novel design of sulfur-doped nickel cobalt layered double hydroxide and polypyrrole nanotube composites from zeolitic imidazolate Framework-67 as efficient active material of battery supercapacitor hybrids. *J Colloid Interface Sci* 628(Pt A):540–552
69. Yang Z, Cheng Q, Li W, Li Y, Yang C, Tao K, et al. Construction of 2D ZIF-derived hierarchical and hollow NiCo-LDH “nanosheet-on-nanosheet” arrays on reduced graphene oxide/Ni foam for boosted electrochemical energy storage. *Journal of Alloys and Compounds*. 2021;850.

Publisher's Note Springer Nature remains neutral with regard to jurisdictional claims in published maps and institutional affiliations.